Int. J. Heat Mass Transfer. Vol. 27, No. 5, pp. 705–716, 1984
Printed in Great Britain

0017–9310/84 $3.00 + 0.00

HEAT TRANSFER DURING INWARD MELTING IN A HORIZONTAL TUBE

C.-J. Ho and R. Viskanta
School of Mechanical Engineering, Purdue University, West Lafayette, IN 47907, U.S.A.

(*Received* 7 *May* 1983 *and in revised form* 19 *August* 1983)

Abstract—Inward melting in a horizontal cylindrical capsule was studied experimentally and analytically. The shadowgraph technique was used to measure the local heat transfer coefficients at the heat source surface. The solid–liquid interface motion during phase change was recorded photographically. The convective motion in the liquid during melting was visualized using aluminum powder as a flow tracer. The experimental results reaffirmed the dominant role played by the natural convective fluid motion in the melt during the inward melting in the tube. In addition to the major natural convective recirculation flow in the liquid, secondary vortex circulation occurred at the bottom part of the melt region. To support the experiments, the data were compared with the numerical predictions and were found to be in good agreement.

NOMENCLATURE

- b location of heated boundary (wall), see Fig. 1
- c specific heat of liquid
- Fo Fourier number, $\alpha t/r_0^2$
- g acceleration due to gravity
- h heat transfer coefficient
- Δh_f latent heat of fusion
- k thermal conductivity of liquid
- Nu Nusselt number, hr_0/k
- $\overline{Nu}$ average Nusselt number, $\bar{h}r_c/k$
- Pr Prandtl number, ν/α
- Ra Rayleigh number, $g\beta(T_w - T_m)r_0^3/\nu\alpha$
- r radial coordinate, see Fig. 1
- r_c characteristic radius defined by equation (16)
- r_0 radius of tube, see Fig. 1
- s solid–liquid interface position, see Fig. 1
- S_c subcooling parameter, $c_s(T_f - T_i)/\Delta h_f$
- Ste Stefan number, $c_l(T_w - T_f)/\Delta h_f$
- T temperature
- t time
- U dimensionless velocity, ur_0/α
- u velocity component in the r-direction
- V volume or dimensionless velocity, vr_0/α
- v velocity component in the Φ-direction.

Greek symbols

- α thermal diffusitivity of liquid
- B dimensionless location of heated boundary, $b/\pi r_0$
- β temperature coefficient of volume expansion
- Γ dimensionless solid–liquid interface position, $s/\pi r_0$
- η transformation variable, see equation (1)
- θ dimensionless temperature, $(T - T_f)/(T_w - T_f)$
- ν kinematic viscosity of liquid
- ξ dimensionless coordinate, r/r_0
- τ dimensionless time, $Fo\ Ste$
- Φ polar angle, see Fig. 1
- ϕ normalized polar angle, Φ/π
- Ψ dimensionless stream function, ψ/α
- ψ stream function
- Ω dimensionless vorticity, $\omega/r_0^2\alpha$
- ω vorticity.

Subscripts

- f fusion
- i initial
- l liquid phase
- m film temperature
- s solid
- w heated wall.

INTRODUCTION

Phase-change heat transfer such as solidification and melting is not only of practical interest to a wide range of technologies but also in geophysics. The work described in this paper has been motivated by latent heat-of-fusion energy storage, heat pump, and geophysical applications. For example, latent heat storage concepts proposed consider horizontal shell-and-tube heat exchangers with the phase-change material either in the tube or on the shell side [1]. In the classical treatment of the phase-change heat transfer problems [2] convection in the liquid has been neglected, and heat transfer is solely due to heat conduction. More recent experimental evidence has clearly established that both during solidification and melting natural convection in the liquid can have an important or dominant influence on the motion and shape of the phase change boundary and on the rate of heat transfer [3].

There exist several analytical studies on heat transfer during inward melting in a horizontal tube (capsule) [4–6]. However, significant differences exist among the numerical predictions, particularly as far as the development of the secondary vortex circulation in the bottom melt region is concerned. No local heat transfer coefficient data at either the heated surface or the solid–liquid interface have been reported, and the limited and

insufficiently detailed experimental data available [5–7] do not permit the resolution of this and other differences between predictions.

An analysis of natural convection heat transfer during melting inside of vertical and horizontal tubes has been performed [4]. Temperature and velocity profiles, heat transfer, and the melting rates have been reported. A secondary eddy circulation was predicted to occur at the top portion of the melt annulus during melting in a horizontal tube and thereby a concavity appeared at the top of the unmelted solid core. A numerical solution of the problem has also been obtained [5], and a secondary vortex motion was predicted to occur below the unmelted solid core and consequently a concavity appeared in the bottom region of the unmelted solid core. An independently performed numerical analysis of the similar problem by using a body-fitted coordinate transformation method has been reported [6]. Solutions were obtained by a strongly implicit procedure. Interestingly, the results show a secondary vortex motion at the bottom part of the tube for $Ra = 10^6$, but the direction of the vortex circulation appears to be opposite of that predicted by others [5]. As a result, a 'valley-hill-shaped' melting front appeared at the bottom of the solid core. Several experiments with n-octadecane as the phase-change material have also been performed [6]. A three-dimensional (3-D) roll cell was observed in the lower part of the melt annulus. However, the observed melting patterns, particularly at the bottom of the tube, differed significantly from those predicted by the analysis.

In an experimental study of the inward solid–liquid phase change inside a horizontal tube [7], emphasis was on the variation of heat transfer to and from the storage unit using naphthalene as the phase-change material. The results indicated that natural convection was the dominant heat transfer mode during melting, whereas conduction was the sole heat transport mechanism during solidification. However, neither local heat transfer characteristics at the heat source surface nor the natural convection flow field has been explored in the work. Inward solidification of a superheated liquid in a cooled horizontal tube has been studied [8]. It was found that natural convection is important only during the early stages of freezing.

The present study was undertaken to obtain experimental solid–liquid interface position and local heat transfer data during inward melting in a horizontal cylindrical tube (capsule). Such data are needed for developing models to simulate the thermal performance of the capsule-type latent heat-of-fusion energy storage and other systems. The effect of the initial subcooling of the solid on the melting process was also studied by performing melting experiments starting with the solid at a temperature substantially below its fusion point. To support the experiments, a numerical simulation of inward melting inside a horizontal tube was carried out, and the predictions were compared with the experimental data. The emphasis in the work was on the experiments and not on the numerical simulations.

EXPERIMENTS

Test apparatus

The test cell used in the experiments is shown in Fig. 1 and consists of a 50 mm long copper tube, 32 mm I.D., having a wall thickness of 4.8 mm. The tube is closed at both ends by two circular Plexiglas disks. A longer test section would have been preferred. Unfortunately, this would have greatly restricted the use of the shadowgraph method for measuring the local heat transfer coefficients. The outer surface of the copper tube is wrapped with a heating coil which is soldered to the tube. A working fluid is circulated through the coil to impose a constant wall temperature boundary condition at the inside of the copper tube. A Plexiglas tube is used on the outside of the heating coil not only to enclose the test cell but also to reduce the heat losses to the environment. Furthermore, to reduce natural convection from the Plexiglas windows of the test cell a second Plexiglas disk was installed parallel to the first at both ends. The volumetric expansion associated with phase change from solid to liquid is accommodated by two overflow outlets at both ends of the test cell.

The volumetric shrinkage of the liquid during solidification is compensated by a small inlet tube located slightly off-axis of the test cell. This compensating-flow inlet serves also to support the solid core from descending during the experiments. The inner surface temperature of the tube was monitored by six T-type thermocouples embedded around the circumference of the tube. Additional details of the test cell design and instrumentation are given elsewhere [9].

The local heat transfer coefficients at the heated wall were measured using a shadowgraph method. The experimental setup employed here is identical to the one described previously [10], thereby obviating the need for detailed exposition. Experimentally, the shadowgraphic technique for heat transfer measurement involves identification of the heat source surface as a reference position as well as the recording of the deflection of the light beam on the screen after its

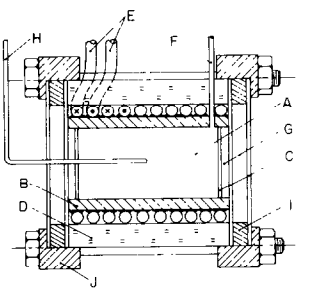

FIG. 1. Schematic diagram of the test cell: (A) test region, (B) copper tube, (C) Plexiglas window, (D) Plexiglas tube, (E) heating coil, (F) overflow outlet, (G) air gap, (H) compensating inlet, (I) collar, and (J) flanges.

passage through the test cell. To make the deflection of the light beam, which passes through the thin region adjacent to the heat source surface, more visible against the dark background, a plate with a narrow aperture was placed between the collimating lens and the test cell. This aperture blocked off the light entering the test cell except that which passed through the immediate vicinity of the heat source surface. The accuracy of the local heat transfer coefficients measured using the shadowgraph system is estimated to be $\pm 10\%$. A Mach–Zehnder interferometer would have been preferred over a shadowgraph. Unfortunately, the high sensitivity of the index of refraction of paraffins to temperature results in too large interference fringe density for accurate interpretation [11], and therefore could not be used for reasonable test surface–fusion temperature differences.

Test procedure and data reduction

Research grade (99% pure) n-octadecane $[CH_3(CH_2)_{16}CH_3]$ was used as the phase-change material in the experiments. This paraffin is desirable because its fusion temperature is near the ambient laboratory temperature, which is conducive for reducing heat losses (or gains) to the environment. Its liquid phase is transparent to the visible radiation, and this allows for the photographic observations and the optical measurements. In addition, the thermophysical properties of n-octadecane are reasonably well established.

The preparation for a test run always began with the degasification of the phase-change material. The material was contained in a flask having a small side-opening and was heated well above its fusion temperature. Then, by connecting the side-opening of the flask to a vacuum pump, the flask was evacuated for about 3–4 h. During this period, the material was allowed to solidify by cooling. After reheating, the degasified liquid was then carefully syphoned into the test cell. The ambient air temperature in the laboratory was controlled such that only a small temperature difference existed between the ambient and the fusion temperature of the material.

Once the test cell was filled with the liquid the shadowgraph system was aligned. A plastic foil marked with a grid network of the exact contour of the test cell was attached on the projection screen to identify the orientation of the heat source. Then, the liquid paraffin in the test cell was solidified by circulating cold (below the fusion temperature) working fluid through the heating coil soldered to the tube. After the solidification was completed the temperature of the circulating fluid was adjusted to a preselected value and maintained thereafter so as to establish an initial temperature condition in the solid for the melting experiments that followed. A uniform initial temperature in the solid was insured by circulating the coolant for a period of about 8 h. After all of these initial preparations, the melting experiment was started by switching on the second constant temperature bath and circulating a hot (above the fusion temperature) working fluid through the heating coil on the outside of the cylinder.

The convective motion in the liquid during melting was visualized using aluminum powder as a flow tracer. Only a very small amount of powder was well mixed with the liquid n-octadecane prior to initiating the solidification of the liquid in the test cell. During the melting experiments, the test cell was illuminated from the front by two lamps located equiangularly with respect to the longitudinal axis of the test cell. The convective flow patterns were visually observed and photographed.

In the experiments, the solid–liquid interface position was photographed at predetermined time intervals. The solid–liquid interface contours as well as the shadowgraph images were photographed with a 35 mm Nikon FE camera on Kodak Tri-X film (ASA 400). The contours of the solid–liquid interface were then traced from the photographs. The area of the unmelted solid was evaluated with a planimeter. The accuracy of this device was estimated to be about $\pm 5\%$ for an area of 1 in^2 (or 6.45 cm^2).

ANALYSIS

Physical model and basic equations

A sketch of the physical model for two-dimensional (2-D) melting inside a horizontal tube is shown in Fig. 2. Initially, the cylinder is filled with solid at its fusion temperature, T_f. At time $t = 0$ the cylinder wall, described by $B(\Phi)$, is suddenly raised to a prescribed temperature ($T_w > T_f$) to initiate inward melting. At any given time t the profile of the solid–liquid interface is assumed to be described by $s(\Phi, t)$.

The analysis assumes that the volume change due to solid–liquid phase transformation is negligible. This implies that the velocity component at the interface perpendicular to the boundary resulting from phase transformation is negligible in comparison to the velocity component parallel to the interface. The experimental evidence available justifies this assumption. The liquid is a Newtonian fluid, and the flow is two-dimensional. The thermophysical properties of the material undergoing phase change are independent of

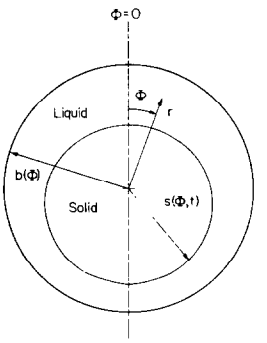

FIG. 2. Schematic diagram and coordinate system for melting inside a horizontal tube.

temperature and are evaluated at the film temperature. The density variation in the liquid is considered only insofar as it affects the buoyancy force, but is otherwise neglected, i.e. the Boussinesq approximation is valid. The idealizations made are identical to those used by others for problems of this type [4–6], and the assumptions appear to be reasonable first-order approximations for the phase-change material used in the experiments.

The dimensionless basic conservation equations (not given here for the sake of brevity) modeling mathematically the moving boundary problem are solved numerically. The Landau immobilization [5] and the body-fitted curvilinear time-dependent coordinate system [6] can be used to accomplish the transformation. The latter scheme appears to be more general, but unfortunately it involves tedious mathematical manipulation to generate the curvilinear coordinate system which increases the computational effort. Therefore, the Landau coordinate transformation defined as

$$\eta = \frac{r - s(\Phi, t)}{b(\Phi) - s(\Phi, t)}, \tag{1}$$

is used in the present analysis. The main utility of this transformation is that the range of η in the transformed space ranges from zero to unity for all r, in the melt region, i.e. the time-dependent physical domain occupied by the liquid in the melt region has been transformed to a time-independent domain. The solid–liquid interface in the transformed space is stationary and given by $\eta = 0$ at any instant of time.

Introducing dimensionless quantities and new coordinates, the transformed version of the governing equations and boundary conditions become:

vorticity equation

$$\frac{\partial \Omega}{\partial Fo} + \frac{\partial \eta}{\partial Fo} + \frac{1}{\pi\xi}\frac{\partial \eta}{\partial \xi}\left[\frac{\partial \Psi}{\partial \eta}\frac{\partial \Omega}{\partial \phi} - \frac{\partial \Psi}{\partial \phi}\frac{\partial \Omega}{\partial \eta}\right] = Pr\,Ra\left[\sin(\phi\pi)\frac{\partial \eta}{\partial \xi}\frac{\partial \theta}{\partial \eta} + \frac{\cos(\phi\pi)}{\pi\xi}\times\left(\frac{\partial \theta}{\partial \phi} + \frac{\partial \eta}{\partial \phi}\frac{\partial \theta}{\partial \eta}\right)\right] + Pr\,\nabla^2\Omega, \tag{2}$$

stream function equation

$$-\Omega = \nabla^2\Psi, \tag{3}$$

energy equation

$$\frac{\partial \theta}{\partial Fo} + \frac{\partial \eta}{\partial Fo}\frac{\partial \theta}{\partial \eta} + \frac{1}{\pi\xi}\frac{\partial \eta}{\partial \xi}\left[\frac{\partial \Psi}{\partial \eta}\frac{\partial \theta}{\partial \phi} - \frac{\partial \Psi}{\partial \phi}\frac{\partial \theta}{\partial \eta}\right] = \nabla^2\theta, \tag{4}$$

where

$$\nabla^2 = \left[\left(\frac{\partial \eta}{\partial \xi}\right)^2 + \left(\frac{1}{\pi\xi}\frac{\partial \eta}{\partial \phi}\right)^2\right]\frac{\partial^2}{\partial \eta^2} + \left[\frac{1}{\xi}\frac{\partial \eta}{\partial \xi} + \frac{1}{(\pi\eta)^2}\frac{\partial^2 \eta}{\partial \phi^2}\right]\frac{\partial}{\partial \eta} + \frac{2}{(\pi\xi)^2}\frac{\partial \eta}{\partial \phi}\frac{\partial^2}{\partial \eta\,\partial \phi} + \frac{1}{(\pi\xi)^2}\frac{\partial}{\partial \phi^2}, \tag{5}$$

$$\frac{\partial \eta}{\partial Fo} = \frac{\partial \Gamma}{\partial Fo}\left(\frac{1-\eta}{\beta-\Gamma}\right), \tag{6}$$

$$\frac{\partial \eta}{\partial \xi} = -\frac{1}{(B-\Gamma)}, \tag{7}$$

$$\frac{\partial \eta}{\partial \phi} = -\frac{1}{(B-\Gamma)}\left[\frac{\partial \Gamma}{\partial \phi} + \eta\left(\frac{\partial B}{\partial \phi} - \frac{\partial \Gamma}{\partial \phi}\right)\right], \tag{8}$$

$$\frac{\partial^2 \eta}{\partial \phi^2} = -\frac{1}{(B-\Gamma)}\left[\frac{\partial^2 \Gamma}{\partial \phi^2} + 2\frac{\partial \eta}{\partial \phi} + \left(\frac{\partial B}{\partial \phi} + \frac{\partial \Gamma}{\partial \phi}\right) + \eta\left(\frac{\partial^2 B}{\partial \phi^2} - \frac{\partial^2 \Gamma}{\partial \phi^2}\right)\right]. \tag{9}$$

The boundary conditions become

$$\phi = 0, 1; \quad \frac{\partial \theta}{\partial \phi} = \frac{\partial U}{\partial \phi} = V = 0, \quad \Omega = \Psi = 0, \tag{10}$$

$$\eta = 1; \quad \theta = 1, \quad U = V = 0, \quad \Psi = 0, \tag{11}$$

$$\eta = 0; \quad \theta = 0, \quad U = V = 0, \quad \Psi = 0. \tag{12}$$

The energy balance at the solid–liquid interface can be expressed as

$$\frac{\partial \Gamma}{\partial Fo} = -Ste\frac{\partial \eta}{\partial \xi}\frac{\partial \theta}{\partial \eta}\left[1 + \left(\frac{1}{\pi\Gamma}\frac{\partial \Gamma}{\partial \phi}\right)^2\right]. \tag{13}$$

Method of solution

A finite-difference numerical method was used to solve the transformed governing equations with the boundary conditions. The equations were discretized and solved on a uniform spaced computational grid network which is fixed in the transformed plane. As a result of compromise between accuracy and computation time required for obtaining solutions, a grid system of 13 nodes in the radial direction by 21 nodes in the polar direction was chosen. Figure 3 illustrates the grid system constructed in the physical plane, which has a smoothly varying grid spacing with a denser grid near the boundaries to account for the boundary layers formed near the solid–liquid interface and the heated wall.

In solving the stream function equation a pseudo-

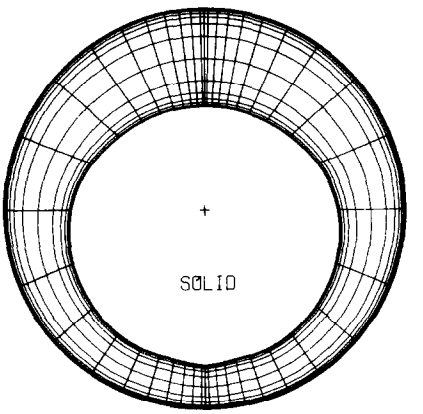

FIG. 3. Grid system (13 × 21) for numerical solution.

transient approach was used by adding a time-dependent term, $(\partial\Psi/\partial Fo)$, to the LHS of equation (3). The alternating direction implicit (ADI) procedure [11] was employed to formulate the system of finite-difference equations in the tridiagonal form. This allowed for their rapid solution by utilizing the well known and efficient Thomas algorithm [12].

Examination of the transformed version of the governing equations and boundary conditions, equation (2)–(13), reveals that the fixed but unknown position of the solid–liquid interface, which is dependent on the unknown temperature field in the liquid, still presents special difficulties for the numerical procedure. An iterative scheme for evaluating this unknown interface has been used for a 2-D phase change of the cylindrical system [14]. However, this scheme is rather time-consuming. A quasi-static approximation was adopted for the present study, i.e. no significant effect of the interface motion on the temperature and flow fields in the melt during short periods of melting was assumed. This assumption is valid for small Stefan numbers, since the interface velocity is much slower than the velocity in the liquid. Two types of approximations (the quasi-stationary and quasi-steady) can be inferred from the above general assumption. The quasi-stationary approximation can be made by simply neglecting the motion of the interface in calculating the velocity and temperature fields in the melt, i.e. the interface position is determined explicitly from the known temperature field at the previous time step. The quasi-steady approximation further simplifies the quasi-stationary assumption by neglecting the transient terms in the governing equations. In general, the quasi-stationary solution is more suitable for the initial melting period due to the rapid motion of the interface and the change of the temperature field with time so as to satisfy appropriate initial conditions. On the other hand, the quasi-steady approximation is ideally suited for long-time behavior in which the interface velocity as well as the temperature and flow fields vary slowly with time.

A combination of the quasi-stationary and quasi-steady approximations was adopted such that the quasi-stationary one was used for initial periods of time and the quasi-steady one for late time. Under the quasi-stationary assumption, the problem reduces to one of a transient natural convection with no phase change. The new solid–liquid boundary is determined from the energy balance condition across the interface, equation (13), based on the temperature distribution obtained at the previous time step. As for the quasi-steady solution, a sequence of steady natural convection states in the melt is determined over a number of larger quasi-static periods of time, during which the interface remains fixed over several time intervals. Typical dimensionless quasi-static intervals taken under the quasi-steady assumption was $\Delta Fo = 3.0 \times 10^{-2}$, which depended on the Rayleigh number and grid size. The time step employed in the computations was determined by stability considerations and depended primarily on the Rayleigh number. For example, for $Ra = 1.2 \times 10^6$ a dimensionless time step $\Delta Fo = 4.0 \times 10^{-6}$ was used. Even with a relatively crude grid the numerical computations were very time consuming, and therefore only two experiments were simulated. Simulation of one experiment required about 43 000 CPU s on a CDC 6500 digital computer.

To avoid potential computational difficulties at $Fo = 0$ [e.g. those associated with $1/(B-\Gamma) \to \infty$, in the governing equations], a very thin, uniform thickness melt layer concentric to the heated wall was assumed to exist initially. The value of Fo corresponding to the assumed melt thickness was determined from the relevant Neumann solution [2]. A typical initial melt layer thickness was chosen to be less than 5% of the radius of the tube. A radially linear temperature distribution across the melt layer was also assumed. The computational procedure using the ADI scheme is given elsewhere [9].

RESULTS AND DISCUSSION

Experimental results

Melting patterns. The photographs of the unmelted solid core contours at different times during the melting yielded a comprehensive history of the melting process. For the range of Stefan numbers examined in this study, the timewise variation of the solid–liquid interface positions during melting are very similar. The melting was uniform along the axis of the tube, because the ends of the test cell were well insulated. The solid maintained contact with the ends of the cell and did not lose support as in some experiments that were reported [17]. If late into an experiment the solid lost support at the ends and descended to the bottom of the cell, the experiment was terminated. One such representative history is presented in Fig. 4. The contours of the solid–liquid interface positions were traced directly from the photographs and are shown at five instants of time during the melting process. At early time ($t = 4$ min), as expected because heat conduction predominates, the interface moves uniformly inward as evidenced by the concentric melt gap. As the melting continues, the onset and intensification of the buoyancy-driven convection in the liquid can be inferred from the presence of the non-uniform inward melting progression. As seen from the figure, the thickness of the melt layer recedes

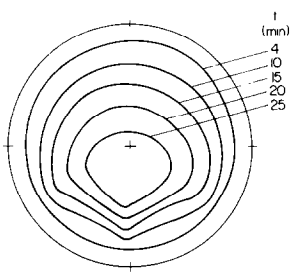

FIG. 4. Timewise motion of the melting front for $Ste = 0.133$ and $S_c = 0.004$.

circumferentially from the top toward the bottom of the cylinder ($t = 10$ min). This is a result of the development of the convective motion in the liquid in which the melt is carried upward along the cylinder wall and gains heat until the top stagnation point of the cylinder ($\Phi = 0°$) is reached. Then, the hot melt flows downward along the solid–liquid interface and looses heat directly contributing to the melting process.

The event of particular interest is the receding trend of the melt propagation velocity which only continues until a certain angular position ($\Phi \approx 123°$), where an abrupt increase of the melting rate takes place as evidenced by a greater displacement of the solid–liquid interface from the cylinder wall. Thereafter, another receding trend of the melting rate starts and reaches a minimum at the bottom stagnation point of the cylinder ($\Phi = 180°$). This unexpected melting behavior is due to the occurrence of strong vortex motion resulting from thermal instability in the bottom part of the melt annulus. Similar observations have also been reported by others [6]. However, in another experimental study [7] on the melting inside a horizontal cylindrical capsule using naphthalene, the material did not show this type of melting pattern at the bottom region of the cylinder. A question of what causes this difference in melting characteristics using two different phase-change materials has arisen and is worthy of further study.

As melting progresses further, the size of the unmelted solid core shrinks markedly. At time $t = 25$ min (Fig. 4), the shape of the solid–liquid interface contour appears to be rather smooth and more streamlined, with a higher melting rate occurring at the top of the cylinder and then decreasing continuously until a minimum is reached at the bottom. This is due to the fact that the thermal instability in the bottom part of the melt annulus tends to be suppressed and is merged to the major convective recirculation flow as the thickness of the melt layer grows with continued heating.

The variation of the molten volume fraction with time, obtained by integrating the solid–liquid interface contours, are presented in Fig. 5. In order to account for the effect of the initial subcooling of the solid on the melting rate, a modified Stefan number, Ste^*, is defined as

$$Ste^* = Ste/(1 + S_c). \tag{14}$$

The dimensionless time $Ra^{1/5}\, Ste^*\, Fo$ was chosen as the abscissa in the figure and correlates the data quite well. The solid line in Fig. 5 is a representation of the correlation obtained through a best least squares fit. The equation for the line is

$$V/V_0 = 0.782(Ste^*\, Fo\, Ra^{1/5})^{0.685}. \tag{15}$$

The dependence on the Rayleigh number indicates that natural convection is the dominant heat transfer mechanism during the melting process. A closer inspection of Fig. 5 further reveals that data points for greater initial subcooling appear to be somewhat more scattered around the correlating line, particularly at the early times.

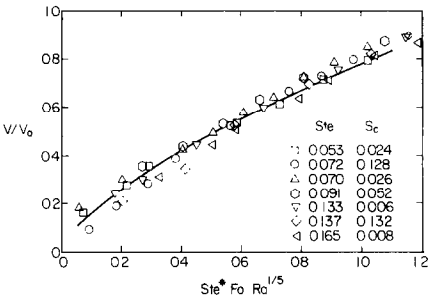

FIG. 5. Correlation for the experimental results for molten volume fraction.

Flow visualization. Several different types of flow visualization techniques (e.g. particles and dyes) have been tried, and the aluminum powder as a flow tracer yielded the best results. The main focus of this flow visualization effort was the bottom part of the melt annulus. Qualitatively evidence of the development of the secondary vortex motion resulted from the thermal instability at the bottom part of the tube can be inferred from the photographs [9]. Closer examination of the photographs revealed that in addition to the major natural convection recirculation flow, which consisted of an upward flow along the tube wall and a downward flow adjacent to the solid–liquid interface, there existed a pair of strong vortex circulations right below the unmelted solid core. It was also evident that the shape of the melting contours in this region appeared to conform with the existing vortex flow pattern. At later times, as the melt layer grew markedly, the intensity of the vortex circulation tended to be suppressed and eventually merged with the major recirculation flow pattern. It appears that the history of the development of the vortex motion in the bottom part of the melt annulus is quite similar to that observed during inward melting in a rectangular cavity with isothermal walls [15].

Heat transfer. Local heat transfer coefficients at the heated wall determined by shadowgraphic measurements are presented in terms of the parameter $Nu/Ra^{1/4}$ vs the polar angle Φ, which is measured clockwise from the top of the cylinder. The radius of the cylinder r_0 was chosen as the characteristic length for both the local Nusselt number Nu and the Rayleigh number Ra. It is realized that this length scale may not be appropriate for all times because the shape and the size of the melt region changes with time.

Figures 6 and 7 present the timewise variation of the local heat transfer coefficients at various angular positions along the cylinder surface for identical Stefan numbers but different initial subcooling parameters. At early times ($\tau = 0.01091$, Fig. 6), conduction is apparently the sole heat transport mechanism as evidenced by the almost uniform local heat transfer coefficient distribution around the cylindrical surface.

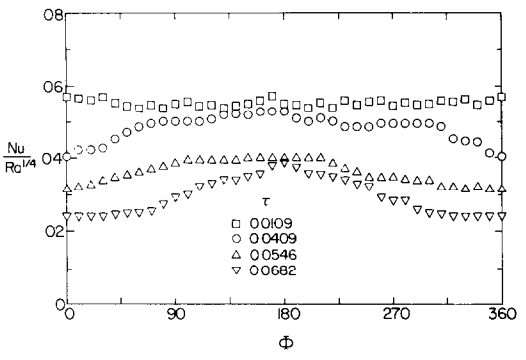

FIG. 6. Variation of the local heat transfer coefficients at the tube wall for $Ste = 0.133$, $S_c = 0.004$ and $Ra = 1.2 \times 10^6$.

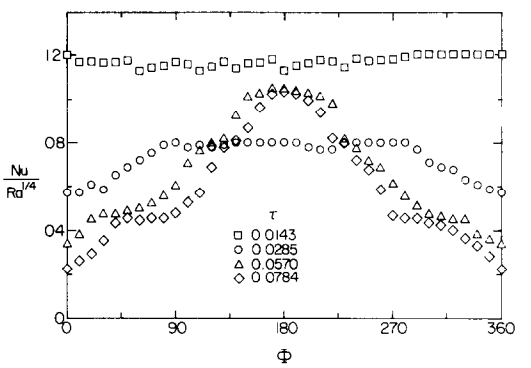

FIG. 8. Variation of the local heat transfer coefficient at the tube wall for $Ste = 0.072$, $S_c = 0.128$ and $Ra = 5.6 \times 10^5$.

As melting proceeds and natural convection develops, the local heat transfer coefficients become nonuniform with a maximum around $\Phi = 180°$ (the bottom of the tube) and a minimum at $\Phi = 0°$ (the top of the tube). Closer examination of the results in Figs. 6 and 7 reveals that the variation of the local heat transfer with angular position and time shows a rather complex trend as a result of competing mechanisms of heat transfer by conduction and convection as well as by the development of the secondary vortex motion in the melt, particularly when there exists significant initial subcooling of the solid (Fig. 7). This may be due to the fact that in the presence of subcooling there is a substantial slowdown in the melting rate, particularly at the early times of the process thereby not only delaying the development, but also decreasing the intensity of the natural convection recirculation.

Figure 8 illustrates the local Nusselt number at the tube wall surface for a lower Stefan number but about the same initial subcooling parameter as the results in Fig. 7. Comparison of the results presented in the two figures shows that there is a larger variation in the local Nusselt number between the maximum value at the top stagnation point and the minimum value at the bottom stagnation point for the smaller Stefan number (Fig. 8). The results also show that a quasi-steady state value of the heat transfer coefficient had not yet been reached.

The average heat transfer coefficient at the heated tube surface is determined by averaging the local values over the circumference of the tube wall. Figure 9 illustrates the effect of the initial subcooling on the average heat transfer coefficient for different Stefan numbers. It can be seen that the larger initial subcooling results in a somewhat higher heat transfer at the surface, particularly at the early times. This can be attributed to the fact that when the solid is initially subcooled part of the energy transported to the solid–liquid interface is conducted across the interface to raise the temperature of the solid. As a result, the melting rate is reduced and with a relatively thin melt layer, a higher temperature gradient exists at the tube wall. Another factor worthy of note in Fig. 9 is that the onset of natural convection and attainment of quasi-steady conditions occurs earlier for higher Stefan numbers. In addition, it is evident that the average heat transfer parameter $\overline{Nu}/Ra^{1/4}$ decreases with increasing Stefan number. A similar trend for the average heat transfer has also been reported earlier [16] for outward melting from a horizontal cylinder.

To obtain an empirical Nusselt–Rayleigh number relationship, it has been found that the experimental data could be best correlated using a characteristic radius r_c defined as [16]

$$r_c = (r_0 r_m)^{1/2} ln(r_m/r_0). \tag{16}$$

In equation (16) r_m is the average instantaneous radius of the unmelted solid core which can be evaluated from the perimeter of the solid–liquid interface, $P = 2\pi r_m$. The experimental results for the average heat transfer

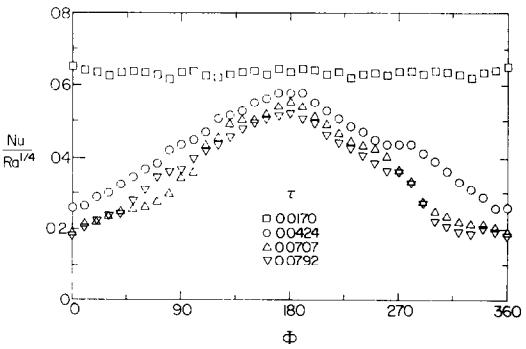

FIG. 7. Variation of the local heat transfer coefficients at the tube wall for $Ste = 0.137$, $S_c = 0.132$ and $Ra = 1.2 \times 10^6$.

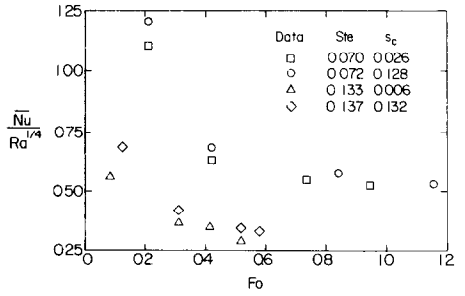

FIG. 9. Timewise variation of instantaneous, circumferentially averaged heat transfer coefficient at the heated tube.

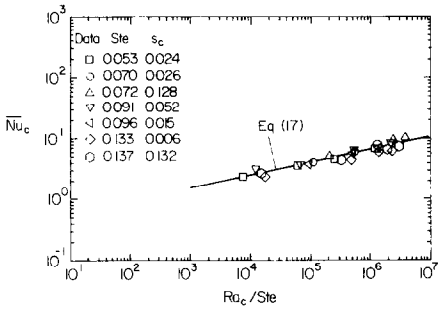

FIG. 10. Average Nusselt number at the tube wall.

coefficients at different Stefan numbers and initial subcoolings are plotted in Fig. 10. The data can be approximated by the empirical correlation based on least squares curve fit of the form

$$\overline{Nu}_c = 0.349(Ra_c/Ste^*)^{0.2125}, \quad (17)$$

where Ste^* is the modified Stefan number defined by equation (14). The data have an average percentage deviation of $\pm 5\%$ from the correlating curve. A correlation of similar form for the average heat transfer coefficients at the solid–liquid interface during outward melting from a horizontal cylinder has also been obtained earlier [16].

Comparison between predictions and experimental data

The fundamental information obtained from the numerical simulations include the solid–liquid interface positions, the temperature distribution as well as information on the flow field in the melt. The heat transfer characteristics were then evaluated from this information. The comparison of the predictions with the experimental data include the melting front profiles, the melting rate, the local heat transfer as well as the average heat transfer coefficient results at the heated tube wall.

Melt shape and volume. Figure 11 shows a comparison between the experimentally determined and predicted melting contours at different times. At early time the agreement is good. At this time, conduction is apparently the dominant heat transfer mode as evidenced by a concentric melting front. As time passes and natural convection develops in the melt annulus, the discrepancy between the measured and predicted melting front positions becomes increasingly greater. The predicted interface velocity at the top of the cylinder is larger than the measured one, whereas the measured solid–liquid interface velocity is greater and the contours differ significantly at the bottom part of the tube from that of the predicted ones. This discrepancy in the melting behavior is attributed primarily to the occurrence of strong secondary vortex circulation in the bottom portion of the melt annulus during the experiments. The presence of this vortex circulation affects the major natural convection flow patterns and thereby the melting behavior. Other possible factors for the discrepancy could be the neglect of the volumetric expansion associated with phase change from the solid to the liquid in the mathematical model, the inherent uncertainty in the thermophysical properties of the material, and non-Newtonian behavior of the liquid at the interface. The buildup of truncation errors with time due to an insufficiently fine grid used may also have contributed to the discrepancy. In order to assess the truncation errors, the grid was increased from 13×21 to 21×21, and good agreement was obtained between the two results; however, the calculations were not carried out for long simulation times.

The predicted instantaneous molten volume fraction is determined from the calculated solid–liquid interface positions and is defined as

$$V/V_0 = 1 - \frac{2}{V_0}\int_0^1 \int_0^{\Gamma} \Gamma(\phi, Fo)\, d\Gamma\, d\phi. \quad (18)$$

Figure 12 gives a comparison between the predicted and measured molten volume fractions. It is evident from the figure that the predicted melting rate is somewhat higher at late times. Despite the great discrepancy between the observed and predicted melting patterns, the agreement between the predicted and measured instantaneous melted volume fraction appears to be fairly good. This is in the main part due to the fact that the predicted and measured solid regions are displaced by about the same amount (Fig. 11) and the fact that comparisons of melt volume are less critical

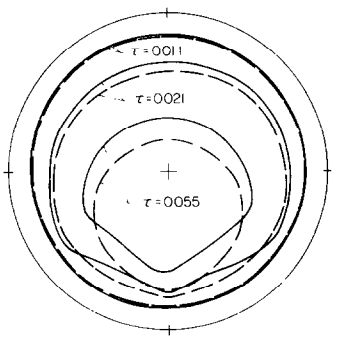

FIG. 11. Comparison of the predicted (dashed lines) melting front profiles with experimental results (solid lines) for $Ste = 0.133$ and $Ra = 1.2 \times 10^6$.

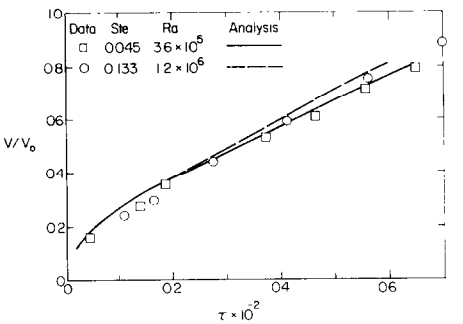

FIG. 12. Comparison of the predicted and measured molten volume fraction as a function of dimensionless time.

than those of the melt shape. Thus, even though the interface contours do not match well, the volume fractions agree much more closely.

Heat transfer. Timewise variation of the predicted isotherms and streamlines for the two different Stefan numbers considered in the simulation are very similar. Figure 13 illustrates predicted streamlines and temperature in the melt region during numerical simulation of the melting process for a Stefan number of 0.133. The contours of the streamlines and the isotherms in the melt are depicted on the left half and the right half of the cylinder, respectively. The formation of boundary layers adjacent to the solid–liquid interface as well as along the heated tube wall can be inferred from the examination of the isotherm and streamline contours in the melt at different times.

At early time [Fig. 13(a)] the isotherms are evenly spaced in the melt annulus, which is indicative of the dominant role played by conduction at this time. Later [Fig. 13(b)] the isotherms are beginning to group together near the top portion of the solid–liquid interface as well as along the bottom part of the tube wall, and boundary layers start to develop. As melting continues, the boundary layer and natural convection circulation patterns appear to be well established [Fig. 13(c)]. It is evident that the temperature is rather uniform across the central layers of the melt annulus, but sharp gradients exist adjacent to the solid–liquid interface and the cylinder wall. Further inspection of Fig. 13(c) reveals that most of the melt near the top of the tube is at a rather uniform temperature which is close to the wall temperature. As a result of this and less steep temperature gradients in the region, a relatively stagnant liquid zone is formed as seen from the streamlines. Similar development of a stagnant melt zone at the top of the cylinder was also predicted by others [4–6]. As melting progresses further, a

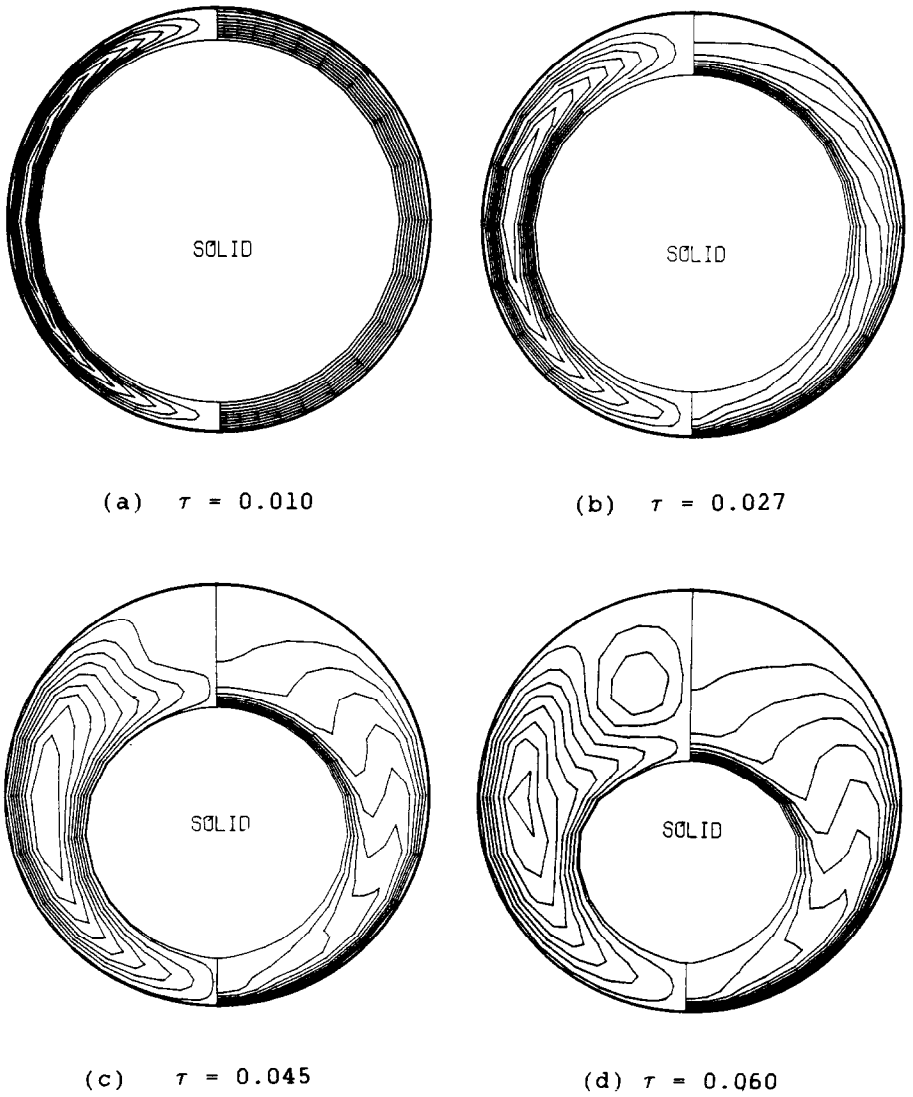

FIG. 13. Predicted distribution of streamlines (left) and of isotherms (right) at various times for $Ste = 0.133$ and $Ra = 1.2 \times 10^6$.

secondary circulation is induced in this region [Fig. 13(d)]. The direction of this secondary circulation is opposite to that of the major natural convection flow in the melt annulus. Although the secondary circulation tends to intensify with time, it appears to be confined in the region near the top of the tube. As a result, the shape of the solid–liquid interface at the top still appears to be smooth and streamlined. This result is in contrast to a concavity predicted at the top of the unmelted solid core [4].

During the flow visualization studies conducted, an attempt was made to clarify the flow field at the top of the cylinder. A stagnant melt zone at the top of the cylinder was indeed observed [9]. As for the secondary recirculation, the flow visualization technique employed in this study could not yield clear and conclusive evidence of its presence. Other possible factors for the difficulty in visualizing the secondary circulation could be the very small velocities in the region and the fact that the flow is not well organized. The magnitude of the predicted velocities in the region is approximately 0.02 cm s^{-1}.

Figure 14 depicts the comparison between the predicted local heat transfer coefficients with the experimental data along the tube wall. The discrepancy between the analysis and the measurements as shown in the figure is considerably greater than the estimated accuracy of the measurement and is mainly attributed to the occurrence of the strong, 3-D vortex fluid motion in the bottom part of the melt annulus during the experiments. This is the region where the discrepancy between the data and analysis is the greatest. This motion greatly affects the natural convection recirculation patterns in the melt and thus the local heat transfer distribution around the inside of the tube wall. The average heat transfer coefficients at the solid–liquid interface Nu_s and at the heated cylinder wall Nu_w are evaluated from the calculated temperature distribution in the melt as

$$\overline{Nu}_w = -\int_0^1 \frac{\partial \eta}{\partial \xi}\frac{\partial \theta}{\partial \eta}\,d\phi, \tag{19}$$

and

$$\overline{Nu}_s = -\frac{1}{\Gamma_s}\int_0^1 \frac{\partial \eta}{\partial \xi}\frac{\partial \theta}{\partial \eta}\left[1+\left(\frac{1}{\pi\Gamma}\frac{\partial \Gamma}{\partial \phi}\right)^2\right]^{1/2}\Gamma\,d\phi, \tag{20}$$

where the quantity Γ_s in equation (20) denotes the length of the solid–liquid interface contour. A comparison of the experimental data with predictions for the average heat transfer coefficients at the heated cylinder surface is depicted in Fig. 15. The analysis shows a sharp decrease of Nu_w at the early times during the melting process. This is indicative of transient heat conduction. As melting progresses, natural convection develops and the average heat transfer coefficient first reaches a minimum and then rises again for a certain period of time. At still later times, as the melt gap becomes wider, the average heat transfer coefficient at the heated surface passes through a local maximum and

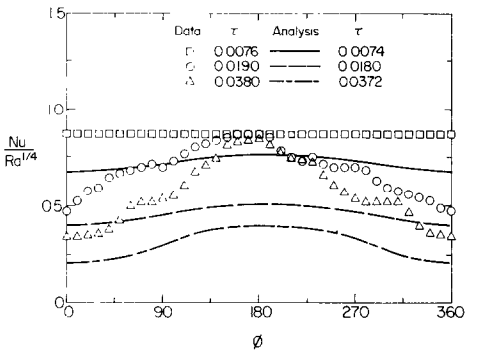

FIG. 14. Comparison of predicted and measured local heat transfer coefficients around the tube wall for $Ste = 0.045$ and $Ra = 3.6 \times 10^5$.

begins to decline gradually until a quasi-steady value is reached. The experimental results show that following the sharp decrease at early times, the heat transfer continues to decrease gradually toward a quasi-steady value without the indication of the local maximum as predicted numerically. It is also clear that there exists a significant discrepancy (about 30% at early times) between the numerically predicted and measured average heat transfer coefficients. This discrepancy between the measured and predicted heat transfer results could be attributed to the failure of the mathematical model to predict the experimentally observed strong vortex circulation in the bottom part of the melt annulus.

The predicted average Nusselt numbers at the solid–liquid interface [14] show continuous increase after a minimum value has been reached at about $\tau = 0.015$. This increase is attributed to the decrease of the heat transfer area of the unmelted solid core and was also predicted by others [6].

CONCLUSIONS

The occurrence of a strong vortex circulation at the bottom part of the melt annulus during melting in a horizontal cylindrical capsule has been qualitatively observed. The presence of this vortex circulating flow significantly affects the melting patterns as well as the heat transfer characteristics at the heated tube wall. As the melt zone grows the intensity of this vortex motion

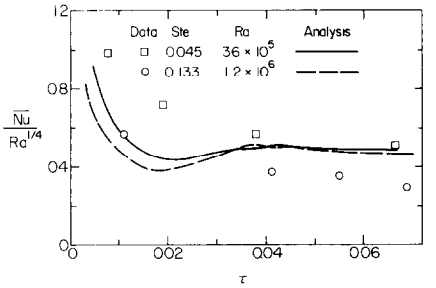

FIG. 15. Comparison of predicted and measured average heat transfer coefficients at the tube wall as a function of dimensionless time.

tends to decrease and eventually merges with the major convective recirculating flow in the melt.

The initial subcooling of the solid during melting inside a horizontal cylindrical tube affects not only the melting rate but also the local heat transfer coefficients.

The 2-D, numerical simulation of the inward melting in a horizontal cylindrical tube was unable to predict the vortex circulation which was observed experimentally at the bottom part of the melt annulus. In this region the flow is three-dimensional. More sophisticated flow visualization experiments and/or velocity measurements using an LDA system and detailed temperature data are needed for the purpose of verifying numerical models. The numerical results obtained with a relatively crude (13 × 21) grid should be considered preliminary. Much more efficient algorithms are needed for solving numerically realistic moving boundary problems of the type considered here.

Acknowledgements—The work described in the paper was supported by the National Science Foundation Heat Transfer Program under Grant MEA-8014061.

REFERENCES

1. R. Viskanta, Phase-change heat transfer, in *Solar Heat Storage: Latent Heat Materials* (edited by G. A. Lane), Chap. 5. CRC Press, Boca Raton, Florida (1983).
2. H. S. Carslaw and J. C. Jaeger, *Conduction of Heat in Solids* (2nd edn.). Clarendon Press, Oxford (1959).
3. K. T. Yang and J. R. Lloyd (editors), *Proc. Natural Convection Workshop*, Breckenridge, Colorado, 18–21 July 1982, University of Notre Dame, Notre Dame, Indiana (1982).
4. J. Pannu, G. Joglekar and P. A. Ricc, Natural convection heat transfer to cylinders of phase change material used for thermal storage, *A.I.Ch.E. Symp. Ser.* **76**(198), 47–55 (1980).
5. T. Saitoh and K. Hirose, High-Rayleigh number solutions to problems of latent heat thermal energy storage in a horizontal cylinder capsule, *J. Heat Transfer* **104**, 545–553 (1982).
6. H. Rieger, U. Projahn, M. Bareiss and H. Beer, Numerical and experimental study of heat transfer during melting inside a horizontal tube, in *Heat Transfer—1982* (edited by U. Grigull, E. Hahne, K. Stephan and J. Straub), Vol. 2, pp. 375–380. Hemisphere, Washington, DC (1982).
7. K. Katayama, A. Saito, Y. Utaka, A. Saito, H. Matsui, H. Maekawa and A. Z. Saifulla, Heat transfer characteristics of the latent heat thermal energy storage capsule, *Solar Energy* **27**, 91–97 (1981).
8. R. Viskanta and C. Gau, Inward solidification of a superheated liquid in a cooled horizontal tube, *Wärme- und Stoffübertragung* **17**, 39–46 (1982).
9. C.-J. Ho, Solid–liquid phase change heat transfer in enclosures, Ph.D. thesis, Purdue University, West Lafayette, Indiana (1982).
10. A. G. Bathelt, R. Viskanta and W. Leidenfrost, An experimental investigation of natural convection in the melted region around a heated horizontal cylinder, *J. Fluid Mech.* **90**, 227–241 (1979).
11. P. D. Van Buren and R. Viskanta, Interferometric measurement of heat transfer during melting from a vertical plate, *Int. J. Heat Mass Transfer* **23**, 568–571 (1980).
12. D. W. Peaceman and H. H. Rachford, Jr., The numerical solution of parabolic and elliptic differential equations, *J. Soc. Ind. Appl. Math.* **23**, 28–41 (1955).
13. C. F. Gerald, *Applied Numerical Analysis*. Addison-Wesley, New York (1978).
14. J. L. Duda, M. F. Malone, R. H. Notter and J. S. Vrentas, Analysis of two-dimensional diffusion controlled moving boundary problems, *Int. J. Heat Mass Transfer* **18**, 901–910 (1975).
15. C.-J. Ho and R. Viskanta, Experimental study of melting in a rectangular cavity, in *Heat Transfer—1982* (edited by U. Grigull, E. Hahne, K. Stephan and J. Straub), Vol. 2, pp. 369–374. Hemisphere, Washington, DC (1982).
16. A. G. Bathelt and R. Viskanta, Heat transfer at the solid–liquid interface during melting from a horizontal cylinder, *Int. J. Heat Mass Transfer* **23**, 1493–1503 (1981).
17. D. Nicholas and Y. Bayazitoglu, Heat transfer and melting front within a horizontal cylinder, *J. Solar Energy Engng* **102**, 299–232 (1980).

TRANSFERT THERMIQUE PENDANT LA FUSION PENETRANTE DANS UN TUBE HORIZONTAL

Résumé—On étudie expérimentalement et analytiquement la fusion pénétrante dans une capsule cylindrique horizontale. La technique des ombres est utilisée pour mesurer les coefficients de transfert thermique locaux à la surface. Le mouvement de l'interface solide–liquide pendant le changement de phase est filmé. Le mouvement de convection dans le liquide pendant la fusion est visualisé en utilisant de la poudre d'aluminium comme traceur. Les résultats expérimentaux réaffirment le rôle dominant du mouvement de convection naturelle dans le bain pendant la fusion dans le tube. En plus de la recirculation de l'écoulement principal dans le liquide, une circulation secondaire tourbillonnaire apparait dans la partie inférieure de la région fondue. Pour confirmer les résultats, les données sont comparées avec les calculs numériques et elles sont trouvées en bon accord.

WÄRMEÜBERGANG BEIM SCHMELZEN IM INNEREN EINES WAAGERECHTEN ROHRES

Zusammenfassung—Der Schmelzvorgang im Innern einer horizontalen zylindrischen Kapsel wurde experimentell und analytisch untersucht. Mit Hilfe der Schattenschlierenmethode wurden die örtlichen Wärmeübergangskoeffizienten an der Oberfläche der Wärmequelle bestimmt. Während des Phasenübergangs wurde die Bewegung der Phasengrenze fotografisch festgestellt. Die Konvektionsbewegung in der Flüssigkeit beim Schmelzen wurde mit Aluminiumpulver als Strömungsindikator sichtbar gemacht. Die experimentellen Ergebnisse bestätigen die dominierende Rolle der freien Konvektionsströmung des geschmolzenen Fluids beim Schmelzvorgang im Innern eines Rohres. Zusätzlich zur Hauptrichtung der freien Konvektionsströmung in der Flüssigkeit erscheint eine Sekundär-Wirbelströmung am unteren Teil des Schmelzgebiets. Um die Experimente abzusichern, wurden sie mit Ergebnissen numerischer Berechnungen verglichen, wobei gute Übereinstimmung festgestellt wurde.

ТЕПЛОПЕРЕНОС В ГОРИЗОНТАЛЬНОЙ ТРУБЕ ПРИ НАПРАВЛЕННОМ ВНУТРЬ ПЛАВЛЕНИИ

Аннотация—Экспериментально и аналитически исследуется направленное внутрь плавление в горизонтальной цилиндрической капсуле. Методом теневой фотографии измерены локальные коэффициенты теплопереноса на поверхности, прилегающей к источнику тепла. Движение границы раздела твердое тело — жидкость при фазовом изменении регистрировалось фотографически. Конвективное движение в жидкости при плавлении визуализировалось с помощью алюминиевого порошка. Экспериментальные результаты подтвердили доминирующую роль свободно-конвективного движения в расплаве при направленном внутрь плавлении в трубе. Помимо основного свободно-конвективного рециркуляционного течения в жидкости происходит вторичная вихревая циркуляция в нижней части расплава. Для проверки результатов экспериментов проведено сравнение с численными расчетами и получено хорошее совпадение.